TEMPERATURE AND COMPOSITIONAL CONTROLS ON TRACE AND REE PARTITIONING BETWEEN CAI-TYPE MELTS AND GROSSITE, MELILITE, HIBONITE, AND OLIVINE: INSIGHTS FROM ISOTHERMAL CRYSTALLIZATION EXPERIMENTS G. Ustunisik[1], D. S. Ebel[1,2], D. Walker[2,1] [1]Department of Earth and Planetary Sciences, American Museum of Natural History (AMNH), New York, NY, 10024 (gustunisik@amnh.org) [2]Department of Earth and Environmental Sciences, Lamont Doherty Earth Observatory of Columbia University (LDEO), Palisades, NY, 10964-8000.

Introduction: The variations in trace and rare earth element (REE) concentrations within individual Ca-, Al-rich inclusions (CAIs) and chondrules can provide information for the formation and alteration of these objects in the solar nebula. Despite most CAIs having complex histories during and after their initial formation [1], high-temperature, Type B (igneous) CAIs [2, 3] offer a unique opportunity to understand the distribution of trace elements in a controlled magmatic system which underwent crystallization from a single starting liquid of a known bulk composition, crystallization sequence [4], and approximately known cooling rate [5, 6]. Melilite and pyroxene have received the most attention in trace element partitioning studies. For example, forsterite bearing Type B3 CAIs have been interpreted to reflect crystallization from molten evaporative residues [7]. Similarly, the REE patterns of coexisting melilites and pyroxenes from some Allende CAI reflect co-crystallization from a melt [8]. On the other hand, [9] concluded that trace element distributions within an Allende type B1 CAI (zoned with melilite-rich mantles) could not solely reflect equilibrium partitioning with a melt [10].

While volatilization, fractional condensation, remelting, fractional crystallization, and subsolidus reequilibration are not mutually exclusive, an accurate assessment of Type B CAIs crystallization requires knowledge of mineral-melt partition coefficients ($^{\text{Min-Melt}}D$) for *all* coexisting phases. Yet $^{\text{Min-Melt}}D$ are only available for certain trace elements and minerals [8-10, 12-14] (e.g., not for grossite [11]) and very limited liquid compositions (mostly CAI-B of [4]).

Here, we designed isothermal crystallization experiments using various bulk compositions from [16] to determine partitioning of trace and REEs in specific fields of condensation space (Fig. 1) between grossite, melilite, hibonite, olivine and CAI-type liquids. These results will provide systematic constraints on compositional and temperature (T) dependence of trace and REE partitioning between solids and CAI-type liquids.

Experimental Design: All experiments were performed at 5 kbar using the bulk compositions in Table 1 in the phase fields of Fig. 1 [15], with a trace element dopant. High-pressure was required to retain the desired volatile trace element abundances in the melt. Six bulk compositions were a mixture of oxides, silicates, and carbonates homogenized in ethanol in an automated mortar for >1 hour and dried at 175°C under vacuum. Dopant was prepared from high purity oxides of La, Ce, Eu, Dy, Ho, Yb, Zr, Hf, Tb, and Ta; carbonates of Sr and Ba; nitrates of Cs and Rb; Th as the mineral thorianite ThO_2; Be as mineral beryl, and B as boric acid H_3BO_3; ground by hand in an agate mortar with ethanol, then decarbonated and denitrified at 1000°C overnight. The dopant mix was diluted with the starting composition of each experiment in several steps to produce 50-100 ppm final concentrations of each trace element, keeping the total trace + REE concentration <1500 ppm so as not to disturb the phase equilibria.

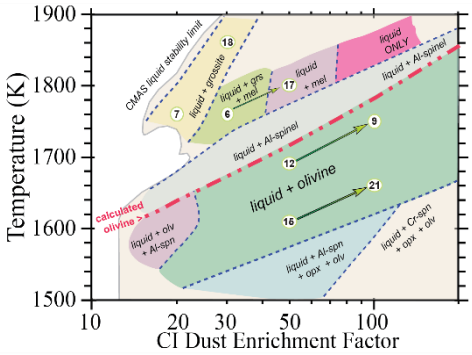

Fig. 1. Experimentally determined phase fields from [15] with the selected compositions used for this study. Figure is adapted from predictions in plate 10 of [16]. Arrows indicate that the two bulk compositions are strikingly similar, although their T differ greatly.

Table. 1. Bulk compositions, and experimental conditions for #6, 17, 7, 18, 9, 12, 15, and 21 along with the stable phases at 5 kbar.

Run#	6	17	7	18	9	12	15	21
SiO_2	19.13	20.37	13.57	5.09	41.28	40.61	44.35	36.06
TiO_2	1.86	1.75	2.05	1.89	0.34	0.37	0.22	0.17
Al_2O_3	43.81	42.75	48.22	59.03	7.79	8.36	4.87	3.78
FeO	0.00	0.00	0.00	0.00	0.27	0.20	0.66	1.02
MgO	1.08	1.71	0.37	0.18	44.10	43.75	46.05	36.17
CaO	34.12	33.81	35.79	33.41	6.16	6.62	3.86	2.99
Total	100	100	100	100	100	100	100	100
Duration (h)	1	1-1.5	25	99	100	111	70	265
T(°C)	1500	1500	1490	1550	1477	1420	1340	1397
Phases	hib geh+liq	hib geh+liq	mel+gr hib+liq	gr+liq	olv+liq	olv+liq	olv+liq	olv+liq

Experiments were conducted at LDEO using piston-cylinder apparatus at the T of interest for each run and 5 kbar for durations of 1 to 265 hours. The assembly was a Pb-wrapped $BaCO_3$/MgO pressure medium, graphite furnace, high-density Al_2O_3 sleeve, one-hole and solid MgO spacers, MgO wafer, and graphite sample capsule, with continuous external H_2-N_2 flow to protect the thermocouple from oxidation. Experiments were typically pressurized cold then heated in slow steps to 850°C over an hour after which the assembly

was left at 850°C, overnight to stabilize and close porosity in the pressure media and graphite capsules. After repressurization, T was raised in steps of ~20 min to the run T, repressurized after 20 min, left for the experiment duration (Table 1), and quenched by turning off the power, cooling to < 400°C in ~5 seconds. Run products were mounted in epoxy, then sectioned and polished for optical examination and quantitative analysis. Major oxide abundances were analyzed using the Cameca SX100 electron microprobe at 20nA beam current and 1µm size for both melt and crystals. Laser ablation ICP-MS (trace elements) standards 614, 612, and 610 were used for trace elements at ≤4 ppm, ≤40 ppm, and ≤400 ppm respectively. A 40-50µm beam size was used for standards and minerals while 25µm was used for finer crystals (e.g. hibonite). Dwell times were 50 millisec (ms) for Li and Be; 25ms for Rb and Cs; and 10 ms for the other trace elements.

Results and Discussion: All runs achieved some thermal compaction: separation of homogeneous glass at the hot top of the capsule and equilibrium phases at the colder bottom. Trace element concentrations within the same run were homogeneous in both glass and each mineral phase. Target final melt trace element concentrations of 50-100 ppm were attained for all except Rb and Cs. **Grossite:** All trace elements were incompatible in grossite (Fig. 2a). This was expected for HFSEs such as Zr, Nb, Hf, Ta, and Th. Boron's incompatibility in grossite, as a LILE, was interesting. Incompatibility of La, Ce, and Eu in grossite was suprising given values for hibonite of [16]: $^{Hib\text{-}Melt}D_{La}$: 4.9-7.2, $^{Hib\text{-}Melt}D_{Ce}$: 3.9-5.2, and $^{Hib\text{-}Melt}D_{Eu}$: 2.8-3.5. The other REEs incompatibility in grossite was similar to that of hibonite. The drop in $^{Gr\text{-}Melt}D$ for grossite (Fig 2a) is qualitatively reasonable but quantitatively larger than expected. **Gehlenite:** La, Ce, Eu, Dy, and Ho were compatible in gehlenite (runs #6, 7, 17) (Fig. 2b). Compatibility of Sr and Ta in gehlenite in #17 and #7 showed the compositional dependence of $^{Geh\text{-}Melt}D_{Sr,Ta}$ at ~1500°C. For both of these runs Th was also compatible in gehlenite. Incompatibility of Th and Yb in runs #17 and #7 might show similar compositional dependence of $^{Geh\text{-}Melt}D_{Th,Yb}$. **Hibonite:** Although La, Ce, and Eu were compatible in hibonite [as in 13], La and Ce were compatible in hibonite only for #7 among all hibonite-bearing runs (#6, 7, 17) (Fig. 2b). Eu is incompatible in hibonite in all three runs. The incompatibility of all elements for hibonite in #6 and #7 compared to #17 might again show the compositional dependence of $^{Hib\text{-}Melt}D$ for ~constant T. **Olivine:** We tested the T-dependence of $^{Olv\text{-}Melt}D$ at similar bulk compositions (comp1: #12 and #9; comp2: #15 and #21; Fig. 1). All trace elements behave incompatibly in olivine and an increase in T (~50°C) seems not to affect $^{Olv\text{-}Melt}D$ for similar bulk compositions, except for $^{Olv\text{-}Melt}D_{Li,Yb}$ (Fig. 2c) which again show a larger jump than expected.

Acknowledgments: This research is supported by NASA Cosmochemistry grant NNX10AI42G (DSE) and the Kathryn Davis Scholarship of the AMNH MAT program (GU).

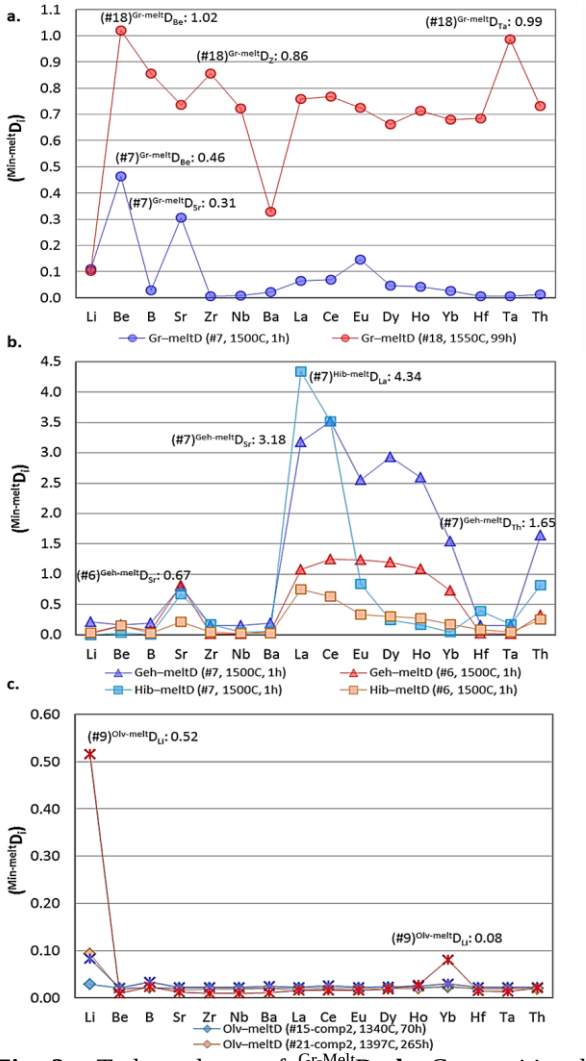

Fig. 2a. T dependence of $^{Gr\text{-}Melt}D_i$. **b.** Compositional dependence of $^{Geh\text{-}Melt}D_i$ and $^{Hib\text{-}Melt}D_i$ at 1500°C. **c.** T dependence of $^{Olv\text{-}Melt}D_i$ at 1420-1477°C and 1340-1397°C for comp1 (#12, 9) and comp2 (#15, 21) respectively.

References: [1] MacPherson G. J. (2004) In *Davis, A.M. (Ed.), Tr. on Geochem.*, 201–246. [2] Boynton, W.V. (1975) *GCA*, 39**,** 56. [3] Grossman L. (1980) *Ann. Rev. Earth Planet. Sci. 8*, 559. [4] Stolper E. (1982) *GCA*, 46, 2159. [5] MacPherson G.J. et al. (1984) *J. Geol*., 92, 289. [6] Stolper E. and Paque J. M. (1986) *GCA*, 50, 1785. [7] Wark et al. (1987) *GCA*, 51, 607. [8] Mason B. and Martin P.M. (1974) *EPSL*, 22, 141. [9] Beckett J.R. et al. (1990) *GCA*, 54, 1755. [10] Kennedy et al. (1997) *GCA*, 61, 1541. [11] Sweeney-Smith S.A. et al. (2010) *LPSC XLI*, Abstract #1877. [12] Nagasawa H. et al. (1980) *EPSL*, 46, 431. [13] Kuehner S.M. et al. (1989) *GCA*, 53, 3115. [14] Lundstrom C.C. et al.(2006) *GCA*, 70, 3421. [15]Ustunisik G. et al. (2014) *GCA*, 42, 27. [16] Ebel D. S. (2006) *MESS 2*, 253.